Towards an advanced modeling of failure mechanisms' interaction in fiber-reinforced polyester: A mixed-mode loading concept

Slah Mzali [a], Ali Mkaddem [b,c,*], Fatma Elwasli [a], Salah Mezlini [a]

[a] Laboratoire Génie Mécanique, École Nationale d'Ingénieurs de Monastir, Université de Monastir, Tunisia
[b] Engineering College, Faculty of Engineering, University of Jeddah, PO. Box 80327, 21589 Jeddah, Saudi Arabia
[c] MSMP-EA7350, Arts et Métiers ParisTech, Rue Saint Dominique, BP. 508, 51006 Châlons-en-Champagne, France

ABSTRACT

This attempt proposes a Finite Element Approach (FEA) to investigate the tribological behavior of glass fiber reinforced polyester composite. The 3D finite element model was developed upon ABAQUS/ Explicit. The Johnson-Cook criteria were considered for describing the material behavior and damage of both fiber and matrix phases. The fiber/matrix interface behavior was, however, modeled using a thin cohesive zone (CZ). A mixed-mode loading concept was specially adopted to predict delamination propagation within the interface. The prevailing wear mechanisms owing to Multi-Scratch Test (MST) were inspected at variable load and attack angle, using scanning electron microscope (SEM). Wear maps were built to highlight the correlation between friction coefficient and wear mechanisms. Predictions of both elementary and interacting mechanisms showed excellent correlation with observations. It was revealed that material removal process varies sensitively with the dominating failure mode. The proposed approach exhibits good ability not only in predicting active mechanisms but also in detecting damage sequences governing the surface integrity during scratching.

© 2016 Elsevier Ltd. All rights reserved.

1. Introduction

The composite materials have become increasingly popular in several industrial sectors such as astronautics, aeronautics, and transports. In addition to their outstanding mechanical properties, the composite materials possess low densities. In several applications, the identification of their tribological behavior i.e. elementary wear mechanisms, friction, lubricant absorption rate, etc. still remain, however, challenging. The anisotropic nature of such materials makes it difficult both the experimental testing and the numerical modeling due to the interaction of elementary mechanisms and difficulty of controlling the interface behavior. The local analysis is mostly used to study the wear mechanisms evolution. In some attempts, the local approach analysis was used to investigate the tribological properties of each composite constituent separately. Scratch test is among the most known techniques used for characterizing tribological behavior of metals [1–3], polymers [4,5], and composites [6,7].

Kim et al. [8] studied the effect of fibers' rate and direction on friction, and wear of short glass fibers reinforced polyamide (PA12) by using a block-on-ring tribotester. They demonstrated that the composite wear rate decreases with the increase of the fibers' amount. A better wear resistance was detected with a composite containing 30 wt% of glass fiber. They also proved the sensitivity of tribological behavior of the composite to temperature and fiber amount.

Using pin-on-disk test, Quintelier et al. [9] investigated the wear mechanisms in glass fiber reinforced polyester (GFRP) composites at dry sliding conditions. They proved that the initial fibers' breakage is always occurring in a cross section regardless of the fiber orientation. In the case of sliding perpendicular to fiber orientation, the initial fiber fracture was attributed to bending causing longitudinal strains. When the fiber orientation is parallel to the sliding direction, high stresses are found to be responsible of the shearing forces. According to the SEM observations, typical composite wear mechanisms, i.e. fiber breaking, fiber/matrix interface debonding, matrix fracture, and fiber pullout, were highlighted.

Wear maps were commonly used in open literature to achieve a better correlation between the tribological parameters and the wear mechanisms [10–12]. Using this analysis technique, Briscoe et al. [13] demonstrated the sensitivity of wear mechanisms to the conical indenter angle and the cure temperature owing to GFRP scratch test. For low angles, it was shown that ductile or

* Corresponding author at: MSMP-EA7350, Arts et Métiers ParisTech, Rue Saint Dominique, BP. 508, 51006 Châlons-en-Champagne, France.
  E-mail address: ali.mkaddem@ensam.fr (A. Mkaddem).

viscoelastic-plastic ploughing switch to a brittle fracture when increasing the cure temperature.

While the experimental approaches, namely, the scratch tests, achieved good conclusions on the single-phase material behavior, i.e. metals, polymers, etc. [14–17], they showed some limitations in accessing all the sought details and local mechanisms dominating the composite material behavior. In particular, the multiplicity of mechanisms acting alone or in complex an uncontrolled interaction makes these approaches not sufficient enough to fully understand the tribological behavior of fiber reinforced polymer composites. However, the finite element analysis (FEA) offers an appreciable alternative because of good modeling flexibility, significant time saving, and high solution accuracy.

Since more than a decade, Goda et al. [18] have developed a micromechanical model for studying the tribological behavior of unidirectional composites using steel asperity-to-composite pair sliding model while sliding was performed perpendicular to fiber orientation. The proposed micro/macro FE approach basing in the modeling of fiber/matrix interface shows much better ability in predicting wear mechanisms than the equivalent macro mechanical approaches widely used in literature [19,20]. According to the predictions, it was revealed that the matrix breaking is due to high shear stress, followed by the formation of a thin film of wear debris. However, the backward fibers' edges in the contacting zone may also crack under high normal stresses. In addition to the prediction of the whole wear mechanisms observed experimentally, the histories of local modes such as matrix shear failure, fiber/matrix debonding, fiber cracking, etc. were successfully highlighted.

Friedrich et al. [21] simulated the sliding of a spherical indenter against GFRP composite sample. When sliding parallel to fiber orientation, it was revealed that fiber/matrix debonding, matrix shearing, and fiber thinning are dominating the wear mechanisms whereas fibers' cracking mechanisms acts in addition to the aforementioned wear modes when sliding perpendicular to fiber orientation. Confrontation of predictions to observations performed on samples scratched by diamond tip proved the validity of simulations.

In spite of appreciable researches have been developed for investigating wear in composite materials, most of them still focused on the SST and neglect, in turn, the effects of physical interactions between active mechanisms that might potentially be of important role in governing local behavior at surface and subsurface.

This paper aims at emphasizing the correlation between tribological parameters and wear mechanisms' interactions basing on micromechanical modeling. Scratch maps were built to highlight the dominating mechanisms and to appreciate the reliability of the numerical predictions.

2. Experimental procedure

2.1. Sample preparation

The sample used in the design of experiments is made of GFRP composite. The material was supplied (supplier: Qinhuangdao Shengze New Material Technology Co., Ltd.) as pultruded rectangular section panels of $1000 \times 50 \times 6$ mm^3 in dimensions. The test specimens were cut at room temperature, under lubrication, at size $50 \times 50 \times 6$ mm^3, using an Al$_2$O$_3$ abrasive grain wheel (Type: PRESI A0) of $\varnothing 230 \times 1.6$ mm in dimensions. The composite material consists of unidirectional E-glass fiber with an average diameter of 23 μm and 21 wt%. The considered composite is, besides, filled with 14 wt% clay filler (ASP400). The scratch tests were performed upon 50×50 mm^2 sample face.

2.2. Scratch tests

Scratch tests were performed using the device whose technical specifications were presented in [22,23]. The testing set up allows varying the different test parameters, namely, the attack angle, the normal load, the scratch velocity and length. A conical uncoated HSS indenter made of W18Cr4V, treated to be at 64 HRC in hardness, was considered for performing the scratch tests [24]. The system ensures the sample target face to be normal to the indenter. Here, both the scratch velocity and length are fixed at 210 mm min^{-1}, and 30 mm, respectively. However, the normal load and the attack angle are taken ranging in 10–50 N, and 10°–60°, respectively. During the test, the tangential load was recorded using piezoelectric transducer connected to an acquisition system. All tests were repeated three times in dry environment and room temperature. In order to appreciate the role of tribological mechanisms' interaction, Multi-Scratch Test (MST) using three aligned indenters with fixed separation distance was confronted to single scratch test (SST). In MST, the equivalent normal load was ensured by three dead weights fixed separately on the indenters. The inter-indenter distance B was kept constant at 1 mm while scratching length was fixed to 30 mm. The apparent friction coefficient (μ_{app}) was calculated referring to Coulomb's law. The wear mechanisms in the two test types were inspected using scanning electronic microscope (SEM).

3. FE modeling

3.1. Assumptions, mesh construction, and B.Cs.

The FE model was developed upon ABAQUS/Explicit code using dynamic/explicit integration scheme. The matrix and the fiber were modeled as separated phases. For predicting debonding mechanisms, the fiber/matrix interface was intentionally modeled by a cohesive zone of 2 μm in thickness [25]. At the difference of literature considering random arrangements [26,27], periodic regular arrangement [28] was assumed herein for building the geometrical composite plate in order to properly control the volume fraction of fibers and to avoid mesh problems. The fibers have hexagonal regular arrangement, average diameter of 23 μm as experimentally inspected by optical microscope, and volume fraction of 34%. Fig. 1a shows the geometry, boundary conditions, and mesh constructions adopted for SST.

In the proposed model, only the zone of interest (ZOI) was simulated using a rectangular parallelepiped of $187 \times 200 \times 800$ μm^3. The upper region where indenter-material contact occurs during scratching, was modeled as multi-phases' material (MPHM) composed of fiber, matrix, and interface phases. Out of the ZOI, the composite was modeled basing on equivalent orthotropic homogeneous material (EOHM) assumption. A total of 20 fibers were used to build the micromechanical sections in SST and MST, respectively. A 3D mesh was generated using the test plate dimensions, where more than 468,142 nodes and a total of 162,948 solid continuum brick elements (type: C3D8R) and 171,828 prism elements (type: C3D6) with linear interpolation between nodes, were used. The mesh discretization was intentionally refined in the vicinity of the indenter at ZOI.

As for SST, only the ZOI was investigated in MST (Fig. 1b) by the reason of rapid convergence. The composite plate was modeled by $2B \times 200 \times 413$ μm^3 parallelepiped, where B is the indenters' separation distance. In order to highlight the effect of interaction, a total of 44 fibers and interfaces were used for building the MPHM section. The model consists of 364,284 nodes connecting 140,980 solid continuum elements (type: C3D8R) and 175,801 prism elements (type: C3D6).
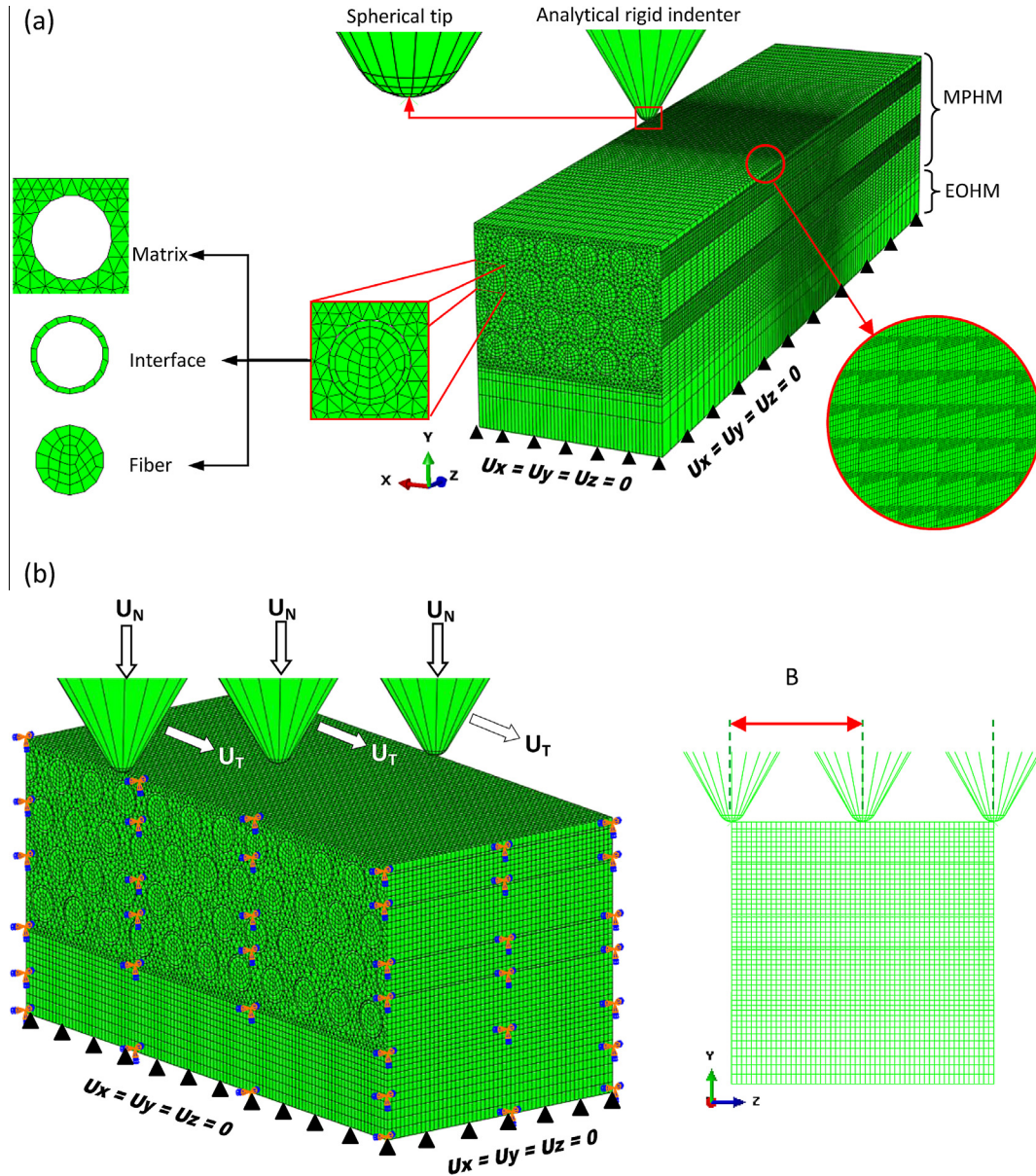
Fig. 1. SST and MST models: mesh construction, indenter position, and B.Cs.

The *contact pairs' algorithm* (surface-to-surface contact) was considered to control the interactions at indenter/fiber and indenter/matrix interfaces while *general contact algorithm* was used to control fiber/fiber and fiber/matrix contact properties. The two algorithms were controlled by the Coulomb law with constant interfacial friction coefficient of 0.125 [29]. However, the behavior at fiber/matrix interface was modeled in SST and MST using 75,828 and 41,764 linear hexahedral cohesive elements (type: COH3D8), respectively. For both SST and MST tests, the numerical convergence was solved within two steps. In a first step, the indenter moves vertically against the fixed plate until reaching the target penetration depth (d_p). In a second step, the scratching starts with the indenter sliding along the specified scratch length ($l_s = 250\,\mu m$). In MST test, the sliding length was intentionally increased so as to overcome the solution instability during scratching step. In both tests, the bottom side of the composite plate was constrained whereas symmetry conditions were applied to left and right sides.

3.2. Material behavior

3.2.1. MPHM section

Both the fiber and the matrix phases were assimilated to disparate homogenous isotropic elastoplastic materials. Especially, glass fiber behavior was determined through standard tensile test provided by Kim et al. [30]. The obtained curve showed a narrow transition zone assumed to be typical plastic zone. Thus, Johnson-Cook constitutive criteria [31] were considered for modeling behavior and damage of composite constituents. Moreover, the Johnson-Cook failure model was chosen because of its ability to relay between plastic strain, strain rate and failure. It, besides, allows thermo-mechanical coupling, if necessary. Its constitutive stress-strain equation is given by:

$$\sigma = \left(A + B\bar{\varepsilon}^{pl^n}\right)\left[1 + C\ln\left(\frac{\dot{\bar{\varepsilon}}^{pl}}{\dot{\bar{\varepsilon}}_0}\right)\right]\left[1 - \left(\frac{T - T_{ref}}{T_{melt} - T_{ref}}\right)^m\right] \quad (1)$$

where σ is the flow stress, A the yield stress at reference strain rate and room temperature, B the hardening modulus, C the strain rate dependency coefficient. $\bar{\varepsilon}^{pl}$ is the equivalent plastic strain, n the strain-hardening exponent, $\dot{\bar{\varepsilon}}^{pl}$ the equivalent plastic strain rate, $\dot{\varepsilon}_0$ the reference strain rate. T, T_{ref}, and T_{melt} are the process, the bulk and the melting temperature, respectively. m is the thermal softening coefficient.

The cumulative damage initiation model is given as,

$$\omega = \sum \frac{\Delta \bar{\varepsilon}^{pl}}{\bar{\varepsilon}_f^{pl}} \tag{2}$$

where $\Delta \bar{\varepsilon}^{pl}$ is the equivalent plastic strain increment, and $\bar{\varepsilon}_f^{pl}$ the equivalent plastic strain at failure, connecting the stress triaxiality with the strain rate and temperature. It is read as:

$$\bar{\varepsilon}_f^{pl} = \left[d_1 + d_2 \exp\left(d_3 \frac{p}{\sigma} \right) \right] \left[1 + d_4 \ln\left(\frac{\dot{\bar{\varepsilon}}^{pl}}{\dot{\varepsilon}_0} \right) \right] \left[1 + d_5 \left(\frac{\theta - \theta_{ref}}{\theta_{melt} - \theta_{ref}} \right) \right] \tag{3}$$

where $d_{i,i\in[1,5]}$ are the failure parameters. The damage evolution is represented by a scalar variable D ranging from 0 to 1. It was described as a linear function of the equivalent plastic strain. The damage evolution is expressed as follows:

$$D = \frac{\bar{u}^{pl}}{\bar{u}_f^{pl}} = \frac{L_{min} \bar{\varepsilon}^{pl}}{\bar{u}_f^{pl}} = \frac{2 G_f L_{min} \bar{\varepsilon}^{pl}}{\sigma_{y0}} \tag{4}$$

$\bar{u}^{pl}$ is the equivalent plastic displacement, L_{min} the minimum characteristic length of the finite element mesh, σ_{y0} the flow stress at the damage initiation, G_f the material failure energy given by:

$$G_f = \int_{\bar{\varepsilon}_0^{pl}}^{\bar{\varepsilon}_f^{pl}} L_{min} \sigma_y d\bar{\varepsilon}^{pl} = \int_{\bar{u}_0^{pl}}^{\bar{u}_f^{pl}} \sigma_y d\bar{u}^{pl} \tag{5}$$

The effects of strain rate, temperature, as well as damage parameters d_2, d_3, d_4 and d_5 are neglected [32]. Table 1 summarizes the fibers and matrix properties, and damage parameters considered in the proposed models.

3.2.2. EOHM section

The elastic constants of the equivalent GFRP composite are determined referring to the approach proposed by Christos and Chamis [35].

$$E_1 = V^f E^f + V^m E^m \tag{6}$$

$$E_2 = E_3 = \frac{E^m}{1 - \sqrt{V^f}\left(1 - \frac{E^m}{E^f} \right)} \tag{7}$$

$$G_{12} = G_{13} = G_{23} = \frac{G^m}{1 - \sqrt{V^f}\left(1 - \frac{G^m}{G^f} \right)} \tag{8}$$

$$\vartheta_{12} = \vartheta_{13} = V^f \vartheta^f + V^m \vartheta^m \tag{9}$$

$$\vartheta_{23} = \frac{E_2}{2 G_{23}} - 1 \tag{10}$$

where E_i, G_{ij}, and ϑ_{ij} are the Young's modulus, the shear modulus, and the Poisson's ratios of the homogenized composite, respectively. i, and j refers to the coordinate systems of the ply. E^f, and E^m are the fibers and matrix Young's modulus, respectively. ϑ^f, and ϑ^m are the fibers and matrix Poisson's ratios, respectively. V^f, and V^m are the fibers and the matrix volume fractions, respectively.

3.2.3. CZ section

Finite cohesive elements were employed to discretize the fiber/matrix interface at MPHM section. The traction-separation concept (Type: QUADS in ABAQUS/Explicit) was selected to simulate failure within the layer. The constitutive theory uses linear elastic behavior coupled with damage initiation and evolution concept. The nominal traction stress vector, **t**, is obtained according to the softening model as:

$$\mathbf{t} = \begin{Bmatrix} t_n \\ t_s \\ t_t \end{Bmatrix} = \begin{bmatrix} K_{nn} & K_{ns} & K_{nt} \\ K_{ns} & K_{ss} & K_{st} \\ K_{nt} & K_{st} & K_{tt} \end{bmatrix} \begin{Bmatrix} \varepsilon_n \\ \varepsilon_s \\ \varepsilon_t \end{Bmatrix} \tag{11}$$

t_n denotes the normal traction, t_s, and t_t refer to the tow shear traction. K_{ij} is the stiffness coefficient, and ε_n, ε_s, ε_t are the nominal, and shear strains, respectively.

The damage initiation is simulated using the quadratic nominal stress criterion. Damage initiates when that criterion, involving nominal stress ratios as given in Eq. (12), reaches a unit.

$$\left(\frac{t_n}{t_n^0} \right)^2 + \left(\frac{t_s}{t_s^0} \right)^2 + \left(\frac{t_t}{t_t^0} \right)^2 = 1 \tag{12}$$

where t_n^0, t_s^0, t_t^0 denote the maximum stresses. Mc-Cauley operator $\langle 0 \rangle$ indicates that damage initiates only under positive stresses, i.e. pure compression causes no damage initiation. Once damage initiates, the degradation of the cohesive element strength is triggered.

The damage evolution resulting in delamination growth uses mixed-mode fracture energy criterion proposed by Benzeggagh and Kenane [36–40]. The fracture is assumed consisting of an opening Mode I (G_I) due to interlaminar tension, a sliding shear Mode II (G_{II}) due to interlaminar shear, and a scissoring shear Mode III (G_{III}) due to anti-plane shear. Delamination is assumed to initi-

Table 1
Input data considered for the numerical proposed models.

MPHM		E (GPa)	ϑ	ρ (kg m^{-1})	A (GPa)	B (GPa)	n	d_1	G_f (J m^{-2})
	Fiber [30]	54	0.21	2550	1.34	15.19	0.99	10^{-7}	500
	Matrix [33,34]	7	0.4	1200	0.049	0.011	0.51	10^{-4}	100
EOHM		E_1 (GPa)	E_2 (GPa)	E_3 (GPa)	G_{12} (GPa)	G_{13} (GPa)	G_{23} (GPa)	$\vartheta_{12}, \vartheta_{13}$	ϑ_{23}
	GFRP	22.98	14.21	14.21	5.18	5.18	5.18	0.33	0.37
Interface		Damage initiation			Damage evolution				
		t_n^0 (GPa)	t_s^0 (GPa)	t_t^0 (GPa)	G_{Ic} (J m^{-2})	G_{IIc} (J m^{-2})	G_{IIIc} (J m^{-2})		
	CZ [34]	0.05	0.075	0.075	10	25	25		

ate when the energy release rate G reaches the fracture toughness of the material $G = G_c$. To predict failure, the three-dimensional failure criterion takes the form:

$$G = G_{Ic} + (G_{IIc} - G_{Ic})\left\{\frac{G_{shear}}{G_T}\right\}^{\eta} \qquad (13)$$

where G_{Ic} and G_{IIc} are pure modes' fracture toughness, $G_{shear} = G_{II} + G_{III}$ the energy release rate for shear loading, and $G_T = G_I + G_{shear}$ the energy release rate under mixed-mode loading [37,38]. The fiber/matrix interface properties used in modeling scratch tests are listed in Table 1.

4. Results and discussion

4.1. Elementary wear mechanisms

Fig. 2 illustrates the SEM micrographs obtained on different samples after scratching tests. It is worth noting that wear mechanisms changes sensitively with the test conditions. The inspections conducted on SST samples highlight the elementary mechanisms resulting in composite behavior, such as fiber fracture, fiber pullout, fiber bending, matrix failure, matrix transverse shear, interface debonding, multi-fracture of fiber, etc. The micrographs show that these mechanisms act alone or in combination with each other depending on scratching conditions. However, it was revealed that there systemically exists a dominant damage mode among all active mechanisms.

From observations, the damage accentuates with normal applied load when relatively small attack angle i.e. 10°. This can be observed by comparing Fig. 2a–c. While series of fracture combining both mode I and mode II failure act at 50 N, simple decohesion and mode II failure dominate under 20 and 30 N, respectively. At lowest attack angle and load (Fig. 2a), no groove was formed since the indenter penetration remains always lower than the matrix superficial layer thickness covering the glass fibers. The superficial fiber layer is compressed under the indenter-tip without causing actual fiber damage. The polyester matrix ploughing seems dominating the wear mechanisms throughout the target surface. Increasing of the normal load to 30 N provokes the transition of prevailing wear mechanisms from ploughing to mode II fiber multi-fractures (Fig. 2b). Under higher normal load, the indenter penetration causes a series of fracture of first fiber layers generating, hence, fiber debris (Fig. 2c).

However, at larger attack angle of 60°, the potential ploughing observed at 10° angle switches to transverse matrix shear while no fiber damage is detected (Fig. 2d). When increasing normal load, deeper grooves occur provoking fiber breaking resulting in neat mode fracture as can be seen in micrographs of Fig. 2e and f. In the two last scratching cases, fiber pullout was also observed which yields, sometimes, fiber/matrix debonding. This was essentially attributed to the indenter penetration that allows the indenter-tip to enter directly in contact with the fibers and pushing it ahead, during sliding, up to final failure.

4.2. Wear mechanisms' interaction

The elementary mechanisms outlined above might interact with each other so as to affect the integrity of scratched surface. Micrographs performed upon MST samples make it possible to highlight the potential interaction between wear mechanisms. Tests were firstly carried out at a constant angle of 60° so as to compare MST-induced mechanisms to SST-induced ones. Fig. 2g–k illustrates the micrographs of multi-indenter induced scratches obtained with 60° attack angle. At lowest normal load, no mechanisms interaction was detected since fiber broke up due to

mode-II dominating failure (Fig. 2g). 10 N load was found not high enough to provoke crack propagation laterally to the scratching direction so as to reach the neighbor groove and, hence, to interact with it. As expected, increasing normal load favors the lateral crack propagation. Hence, mechanisms of adjacent grooves can met and actively interact with each other. Fig. 2h proves the coexistence of interface debonding, fiber pullout and bending with predominant mode-II failure. Interaction being further enhanced with more severe scratching conditions, namely, relatively higher load. In addition to above mechanisms, Fig. 2k reveals the development of matrix local shearing and/or ploughing, and generation of fiber debris. Once, at least, one of selected testing parameters reaches its critical value, these mechanisms will act in full interaction to control the tribological behavior of the target surface.

These latter vary also sensitively with the attack angle. MSTs were conducted at a constant load ($F_n = 30$ N) by the reason of investigating the effects of attack angle in the evolution and interactions of wear mechanisms. Enlarged views obtained on composite sample surface, scratched at three typical angles, i.e. 10°, 30°, and 45° were supplied in Fig. 2l–n.

With an indenter of 10° attack angle, the inspections reveal the presence of fibers debris relatively shorter than those observed with higher angles (Fig. 2l). This means that the fiber sectioning is assumed as neat as the attack angle is low. The orientation of failed debris entails that fibers have potentially already undergone little bending acting in coordination with a pullout mechanisms. In the micrograph of Fig. 2l, the most debris looks consisting of cut fiber embedded into its surrounding matrix phase. Physically, this involves that the interface resists to debonding because of mode-II premature failure preventing, in turn, excessive bending. This former, when being accentuated at higher attack angles (Fig. 2m and n), causes decohesion of fibers from its surrounding matrix due to intensive shearing along a relatively large distance away from the indenter-tip. Hence, when increasing the attack angle, the dominant wear mechanisms switches from "short bending → mode-II fiber failure → insubstantial pullout" to "severe bending → interface shearing → mode-II fiber failure → significant pullout". These observations confirm the sensitivity of wear mechanisms to the attack angle, and provide valuable proof on the role of elementary mechanisms' interaction in controlling failure path of composite phases.

Referring to the inspections, the number of fiber coming into contact with the indenter should rationally increase with increasing the attack angle, which promotes the fiber pullout. Fig. 2m and n exhibit typical stripped fibers after matrix breakage.

4.3. Friction analysis

The apparent friction coefficient is determined as the tangential-to-normal force ratio i.e. $\mu_{app} = \frac{F_t}{F_n}$, where F_t and F_n are the tangential and normal loads, respectively. An acquisition system was employed for recording tangential force component during tests. In MST, μ_{app} refers to the average friction coefficient calculated upon the three indenters. Fig. 3a illustrates the configuration of the three indenters when scratching the composite sample. Fig. 3b shows, however, the evolution of apparent friction coefficients versus attack angle obtained at $F_n = 30$ N. The plots look of similar trends. In domain 1, where relatively small attack angles were used, the mean apparent friction coefficient doesn't exceed 0.2. The data reflects good coincidence between μ_{app}^{MST} and μ_{app}^{SST} values. It appears that the interaction under these conditions has no significant effect. This was essentially attributed to comparable tangential force in the two tests. As explained above, mode-II failure dominates the wear mechanisms in both SST and MST tests (see analysis of micrographs Fig. 2b and l), which lets to assume
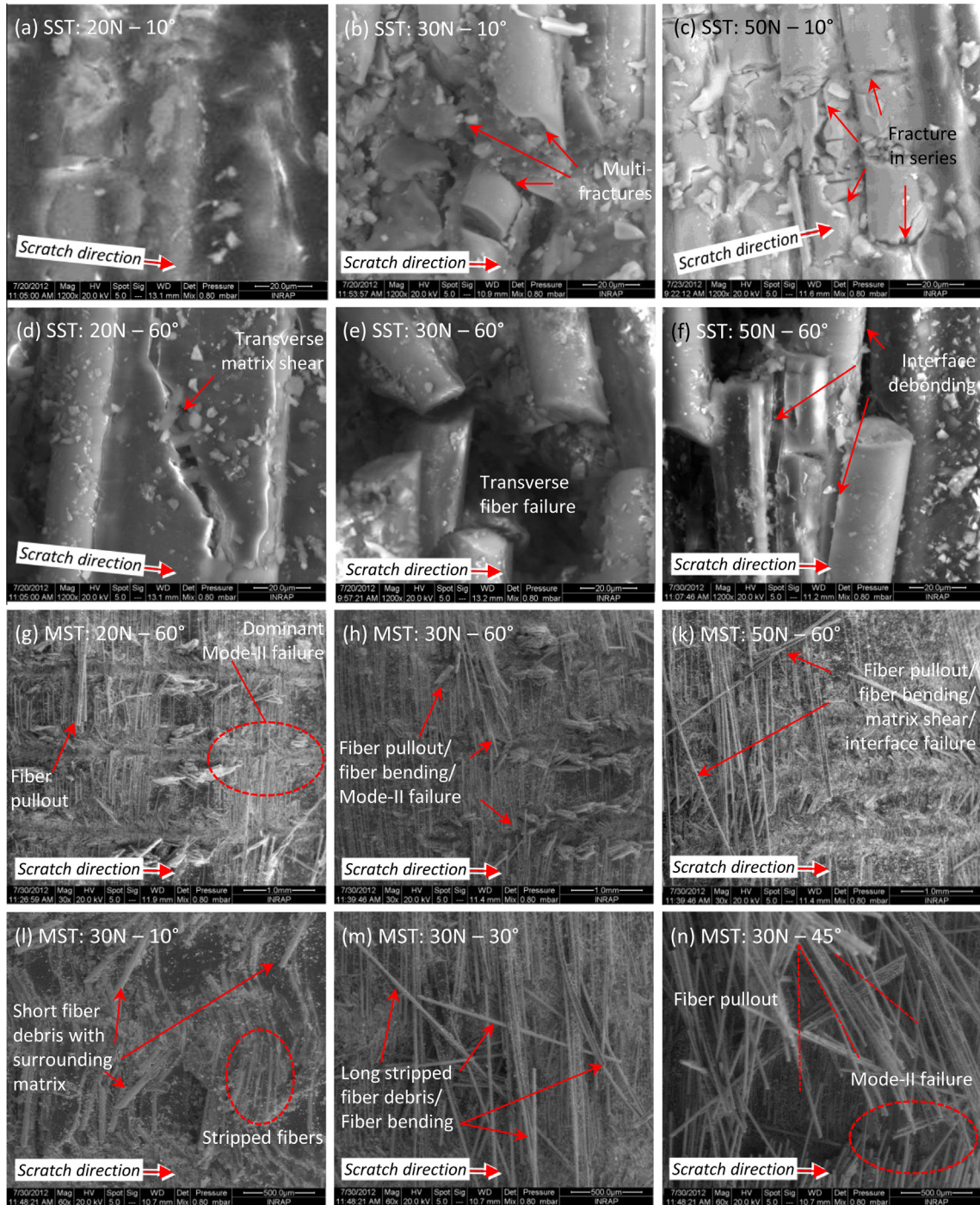
Fig. 2. SEM micrographs highlighting the wear modes under scratch tests. (a–c) SST − $\theta = 10°$, (d–f) SST − $\theta = 60°$, (g–k) MST − $\theta = 60°$, and (l–n) MST − $F_n = 30$ N.

that tangential forces developed in the two tests still remain comparable. The bending mechanisms perceived in MST, should start to act on friction beyond 30° attack angle since only little bending was outlined within domain 1 (see typically, description of mechanisms on Fig. 2l). In that domain, the apparent friction coefficient varies weakly. This is essentially due to the matrix ploughing.

Contrary to aluminum alloy [23], the mechanisms' interaction owing to MST causes unexpectedly a significant fall of friction coefficient while attack angle exceeds 30°, as can be detected in domain 2. The gap between the SST- and MST-induced friction values increases sharply as beyond 30°. The friction ratio, $r = \frac{\mu_{app}^{MST}}{\mu_{app}^{SST}}$,

reaches an average value of 0.51 ± 0.03 within 45–60° attack angle range. This means that μ_{app}^{MST} is approximately a half of μ_{app}^{SST} in that range. However, the tendencies exhibit much sharp slope versus angle below 45° than over that value. The significant decrease in friction was essentially attributed to the transition of the dominating wear mechanisms from fiber fracture to ploughing which should be accentuated over 45°. In the latter region, a slight increase in the apparent friction coefficient of 7% is observed. Otherwise, the effect of the interaction is considerably perceived in domain 2. The sliding of the first indenter (1) yields the material removal due to involved mechanisms acting in combination with each other for causing matrix breakage, transverse fiber failure,
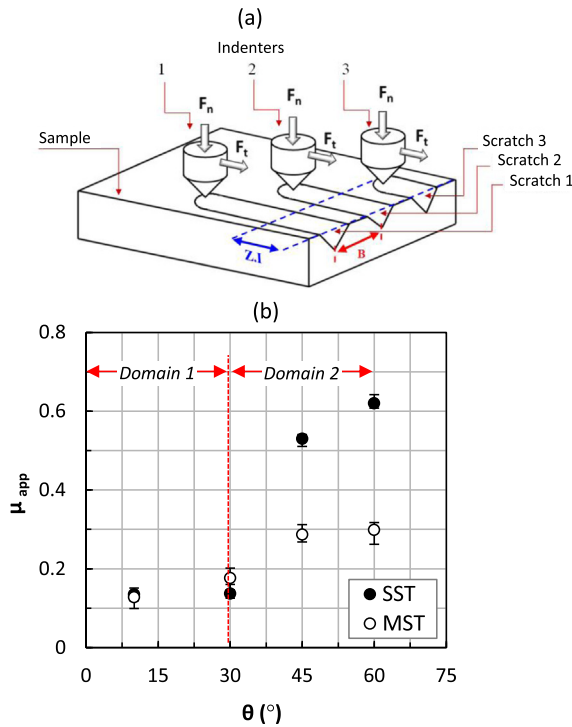
Fig. 3. (a) Illustration of indenters' position in MST, and (b) Evolution of apparent friction coefficient vs. attack angle for a normal load $F_n = 30$ N.

and the fiber/matrix interface debonding. This facilitates, hence, the following indenter (2) to attack the surface at the same penetration depth (d_p), and to remove the material with a lower force. Thus, the last indenter (3) comes into contact with areas being already damaged; the deformation and failure of fibers stripped of their surrounding matrix phase should require a relatively lower tangential reaction force than that developed against the indenter 1 and 2. This favors, in turn, the drop of apparent friction if compared with prior indenter.

4.4. Wear maps

The correlation between the tribological parameters and wear mechanisms should be unveiled to identify the action purview of each mechanisms was already outlined. Therefore, wear maps were drawn in order to emphasize the damage limits resulting in both elementary and interacting mechanisms. Special focus was put on the sensitivity of those mechanisms to attack angle and normal load. From experimental findings, four elementary dominant damage modes were distinguished as shown in Fig. 4a.

- $\theta \leqslant 30°$

For relatively low angles, two wear mechanisms are distinguished dominating; (i) Ploughing, and (ii) fiber multi-fractures. The first one acts within the small load range i.e. [10, 30] N. In that range, the indenter sliding causes neither polyester material removal nor fiber fracture. Only a plastic flow of the matrix occurs. However, the multi-fracture mechanisms acting over 30 N, ranges in a larger area. The crushing of the superficial fiber layer by the action of indenter favors, in turn, the matrix damage, and activates at this stage the fiber/matrix interface debonding. The fracture-in-series of fibers involves free debris at the worn surface (Fig. 2c).
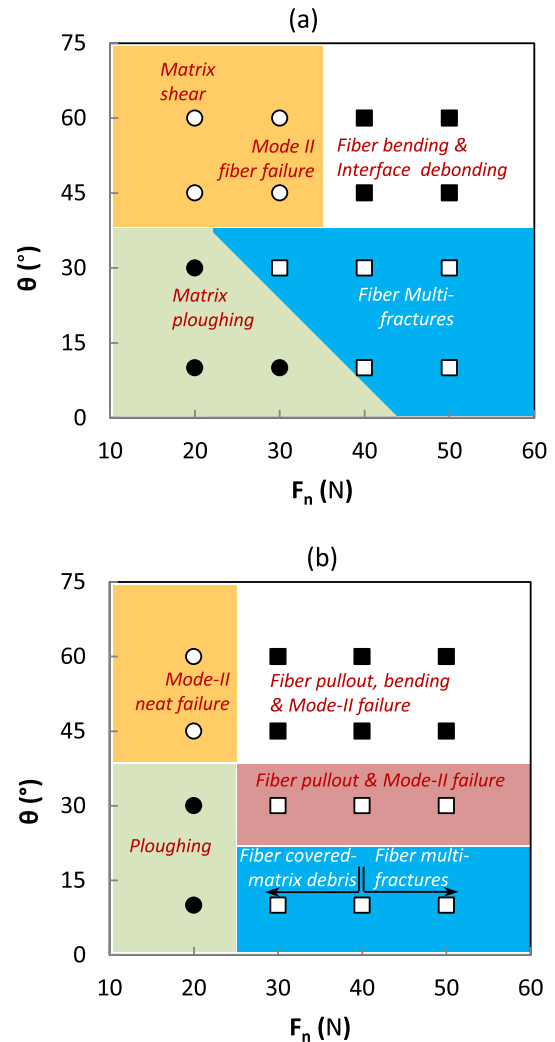
- $\theta > 30°$

Fig. 4. Wear maps built according to SEM observations. (a) SST wear map, and (b) MST wear map.

In this case, the wear mechanisms are more severe. Two modes are dominating the composite behavior, namely, (iii) mode-II fiber failure associated sometimes with matrix shear, and (iv) fiber bending associated with interface debonding. Below 30 N, the indenter advancement causes the rupture of the polyester and the fracture of several fiber layers. Since the indenter penetration increases with increasing the normal load, the indenter-to-superficial fiber layer contact area becomes larger which constrains the fibers to bend and thus to break away from the indenter-tip. In this case, the fiber/matrix interface debonding enhances the fibers pullout. These two dominating mechanisms seem to act in full coordination.

The above elementary mechanisms were, unexceptionally, met in MST while predominately operate in full conjunction. The main domains were classified according to SEM observations into five types as provided in Fig. 4b. The following remarks can be, hence, drawn:

- $10° \leqslant \theta \leqslant 40° - F_N < 25$ N

In this domain where normal load and attack angle are relatively low, matrix ploughing seems to operate separately. The scratches are shallow and narrow enough, which suggests the absence of any interaction.

- $10° \leqslant \theta < 20° - F_N \geqslant 25$ N

In this domain, the wear mechanisms were found very sensitive to the normal load. The mode-II fiber failure, observed in low range of angles, acts so rapidly to prevent bending of constrained fiber and hence avoids relative shearing along fiber/matrix interface. Therefore, failure occurs on the fiber phase together with the surrounding matrix. This was highlighted through the presence of matrix-covered short fiber debris at that domain (Fig. 2l). With increasing normal load ($F_N \geqslant 40$ N), the interaction between grooves promotes fiber multi-fractures which takes place to the detriment of simple mode-II failure.

- $20° \leqslant \theta < 40° - F_N \geqslant 25$ N

Over 30°, mode-II fiber failure dominates in combination with pullout mechanisms favoring generally fiber bending. This latter motivates shear along the fiber/matrix interface causing, hence, separation between the two material constituents before that fiber transverse failure takes place. This looks at the long stripped fiber debris inspected throughout the damaged surface (Fig. 2m).

- $40° < \theta \leqslant 60° - F_N < 25$ N

Within this domain, matrix ploughing that is fully acting in the domain located just bellow ($\theta \leqslant 40 - F_N < 25$ N), transforms to secondary partial ploughing. However, the mode-II fiber failure was found governing the surface wear (Fig. 2g). Fiber pullout phenomenon was also a little detected.

- $40° < \theta \leqslant 60° - F_N \geqslant 25$ N

This is pointed out as the largest domain of the wear map. The relatively high normal load generates deep penetration and forces cracks to propagate laterally to fiber direction. As obvious, this develops interaction between mechanisms propagating from each of the grooves. In fact, the advancement of the first indenter pushes the fiber ahead and causes the interface shear which favors, in turn, the pullout of the fiber layer at the superficial matrix phase. Out of their location, separate fibers as fiber blocks undergo excessive bending before final transverse breaking (Fig. 2n). It is worth noting that the most severe interaction between mechanisms occurs within this domain while mode-II failure controls the final damage set.

4.5. FEA

4.5.1. Predicted vs. observed elementary failure mechanisms
Single-scratch test was intentionally simulated using the highest attack angle, i.e. 60° since this angle reflects, relatively, severe testing conditions as mentioned above (Fig. 2e–f). In fact, under such an angle, the three composite phases namely, fiber, matrix and interface undergo critical damage resulting in various elementary failure mechanisms.

Fig. 5 illustrates typical results obtained at a penetration depth of 100 μm. The predictions were presented together with corresponding SEM observations. The numerical contours show the overall stiffness degradation scalar (SDEG) distribution resulting in the damage variable D. It is noteworthy the good concordance between simulations and micrographs. The dominant fiber failure mode highlighted by SEM inspections was accurately reproduced by the proposed model as can be seen in Fig. 5 a and a'. The fibers were firstly pushed front to the indenter-tip before they fail neatly in the contact zone. The indenter advancement causes the fiber bending followed by *like-stretching* phenomenon owing to large

deformation. This yields fracture not only within the zone of contact with the indenter but also away from this zone. The superficial fiber layers are specially subjected to the former phenomenon since the circumference of the conical indenter is as wide as cross section is far from the indenter-tip. This phenomenon is responsible of the generation of fiber debris during scratching. The numerical isovalues reveal damage localization at the tension zone of the fibers which proves the ability of the model to simulate the substantial mechanisms dominating fibers' failure.

Fig. 5b emphasizes the damage mode involved in the matrix phase. Two mechanisms are typically perceived: longitudinal shear and transverse shear. While sliding against the composite, the indenter generates longitudinal matrix shear towards the scratch direction inducing, hence, material removal. However, stretching the fibers in contact with the indenter involves fiber/matrix interface debonding before causing matrix failure perpendicularly to the scratch direction. Observations (Fig. 5b') promote clearly the reliability of the model to simulate the matrix damage modes, and their location throughout the composite scratched area.

The CZ makes it possible the simulation of fiber/matrix debonding (Fig. 5c). The failure of interface yields generally affected region greater than that generated by fibers or matrix damage where failure significantly localizes. This observation was outlined experimentally through the SEM inspections. The fiber pullout has tendency to deform the matrix which generates, in turn, a wide affected area between the fibers. The separation of the fibers from the matrix allows the loss of surface integrity (Fig. 5c'). The numerical contours within the interface prove the relative agreement with the observations.

4.5.2. Simulation of mechanisms' interaction
Numerical simulations were also conducted to predict whether the elementary damage mechanisms interact under specified conditions. Fig. 6 shows typical damage contours obtained in two extreme scratching cases: negligible interaction and severe interaction.

Fig. 6a illustrates the damage contours involved at $\theta = 60°$ and relatively low normal load ($d_p \rightarrow 25$ μm). As previously reported from observations, mode-II failure was found dominating the damage mechanisms in such testing conditions. The numerical model exhibits shallow streaks presenting in-between insignificant surface damage value ($0.2 \leqslant SDEG \leqslant 0.3$). This entails that material removal process was substantially governed by the elementary mechanisms. SEM observations confirm decidedly the predictions since damage area exhibits a non-affected zone separating two consecutive grooves as can be typically seen in Fig. 6a '. The former zone should reduce with increasing normal load, i.e. increasing d_p. As fiber bending and pullout are inactive in such conditions, matrix failure localizes close to the indenter-tip, along the scratching path. However, matrix flow occurs along the groove boundaries which may progress laterally with increasing normal load for reaching full interaction under critical scratching conditions. Such interaction phenomenon can be, however, clearly perceived for higher attack angle and load.

Fig. 6b proves the qualitative efficiency of the proposed model in predicting material removal due to severe interaction. The damage process was found involving *matrix shear → fiber pullout → fiber bending → mode II fiber failure*. Under the action of the indenter, fiber debris and matrix-covered fiber blocks were thrown out of the tool trajectory (Fig. 6b and b'). At such a load range, not only superficial fiber layers suffer from critical damage but also the layers beneath the tool-tip. In fact, the subsurface layers undergo the local compression generated toward the indenter-tip. At critical
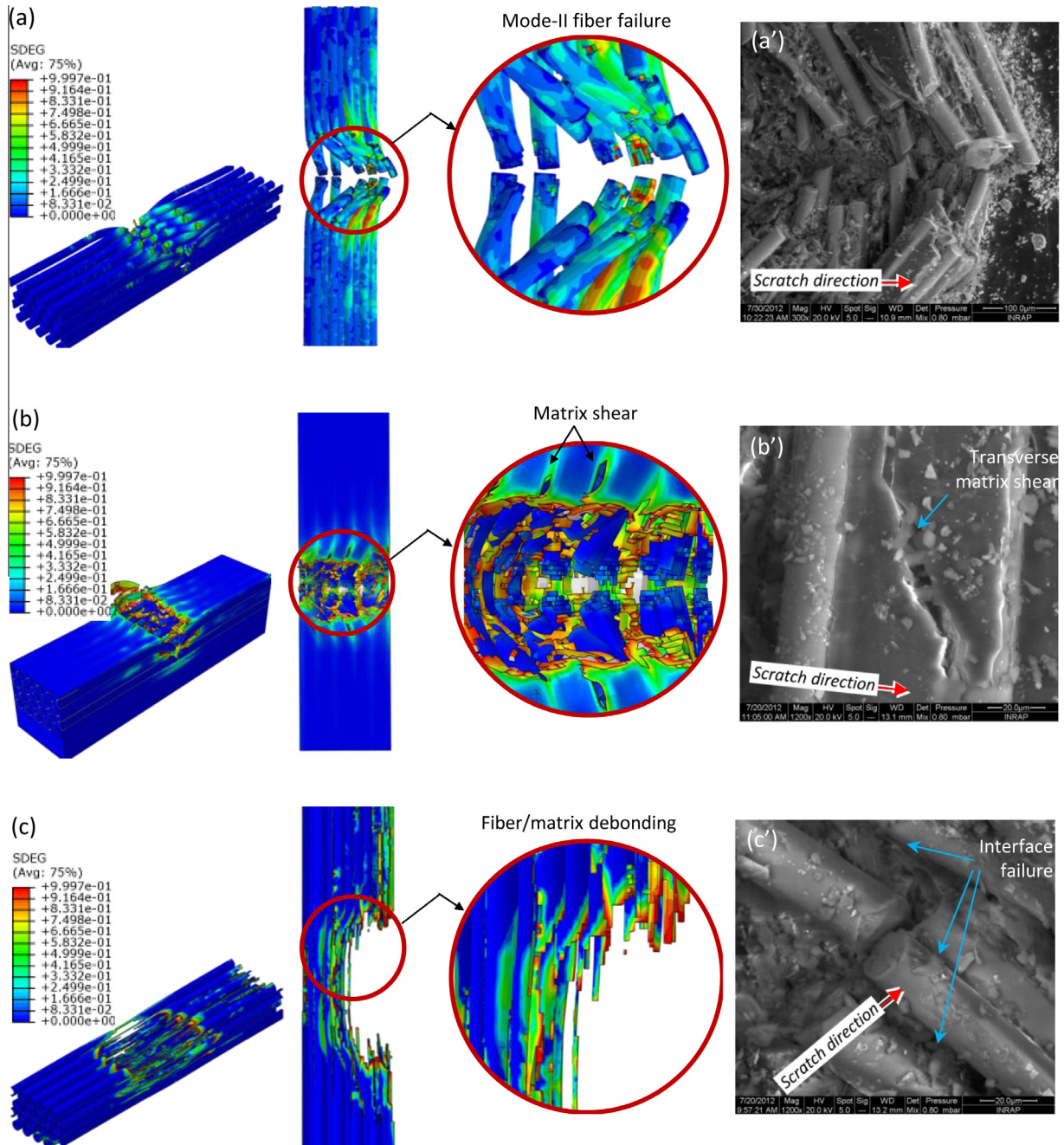
Fig. 5. Typical failure mechanisms predicted using SST model ($\theta = 60°, d_p = 100$ μm). (a–a′) Fiber failure, (b–b′) matrix failure, and (c–c′) interface failure.

compression fields, the subsurface layers might fail affecting therefore the composite integrity. The SEM inspections correlate sensitively with the predictions of catastrophic failure owing to interaction of elementary mechanisms.

5. Conclusions

In this paper, the investigation of elementary wear mechanisms in both SST and MST were carried out. A numerical approach was specially proposed for better understanding of the evolution of damage mechanisms. Particular focus was put on highlighting the effect of mechanisms interaction in the material removal process. According to the findings, the following conclusions can be drawn.

- The SEM observations make it possible to distinguish the elementary mechanisms dominating the material removal process in SST and their limits of action when the testing parameters, namely, the attack angle and normal vary. Inspections of multi-scratched worn area reveal high sensitivity of surface integrity to dominant interacting mechanisms.
- When SST, the apparent friction displays high dependency on tribological parameters. However, it shows more sensitivity to the attack angle than to the normal load. An increase in the attack angle increases μ_{app}, and switches the wear mechanisms from ploughing to fibers pullout and fibers fracture.
- The wear maps reveal that ploughing, fibers multi-fractures, and fibers fracture dominate within smaller domain in MST than in SST. However, the combined fibers fracture and fibers
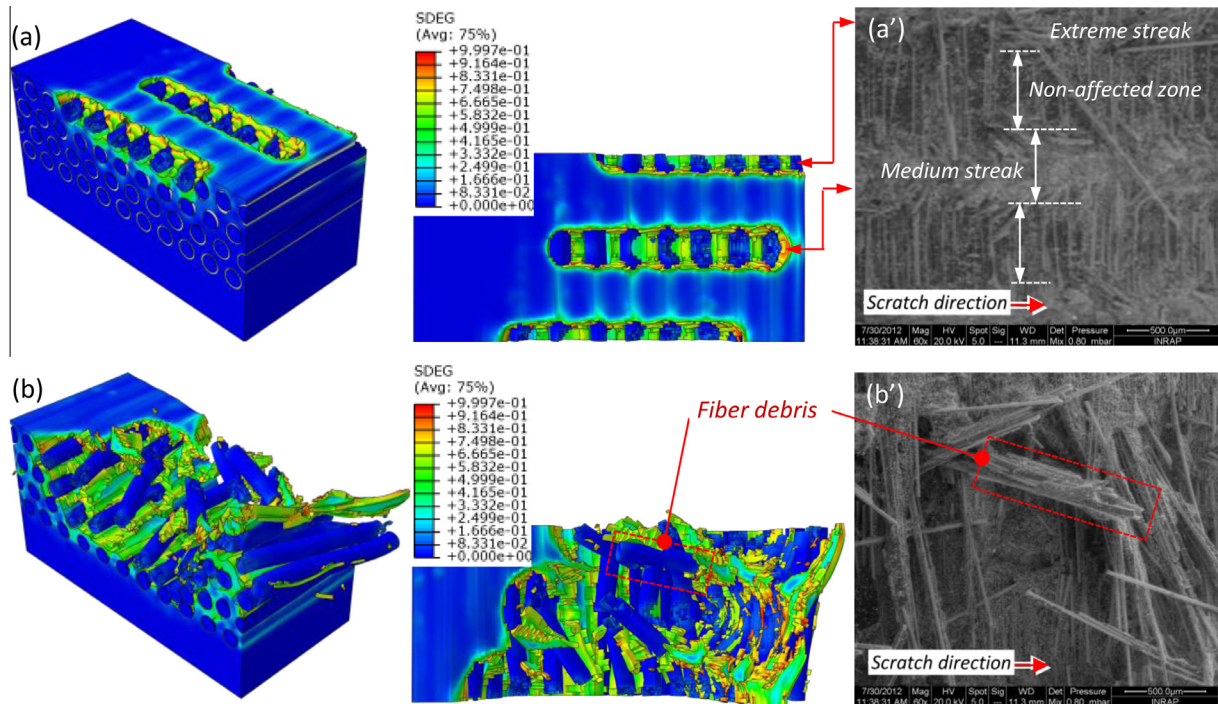
Fig. 6. Typical simulations showing extreme cases of interaction mechanisms involved during MST. (a) $\theta = 60° - d_p \rightarrow 25 \, \mu m$, (a') $\theta = 60° - F_N \leqslant 20 \, N$, (b) $\theta = 60° - d_p \rightarrow 100 \, \mu m$, (b') $\theta = 60° - F_N \geqslant 30 \, N$.

pullout dominant mechanisms occupy a larger domain in MST. Five domains were drawn in MST face to only four domains drawn in SST. Major mechanisms transformation was outlined for relatively high load and low angle ranges: The elementary fiber multi-fractures dominating in SST becomes acting in association with fiber pullout and mode II fiber failure in MST.

- The proposed models exhibit excellent ability to simulate damage mechanisms dominating material removal process in both SST and MST. Specially, the mixed-mode loading criterion shows high efficiency to predict delamination propagation in the CZ. Decidedly, SEM inspections confirmed the numerical results. In fact, the MST model demonstrates ability to predict mechanisms' interaction together with sequences of material removal process in GFRP composite.

References

[1] Rodriguez-Castro GA, Vega-Moron RC, Meneses-Amador A, Jimenez-Dıaz HW, Andraca-Adame JA, Campos-Silva IE, et al. Multi-pass scratch test behavior of AISI 316 l borided steel. Surf Coat Technol 2016;307:491–9.

[2] Xu X, van der Zwaag S, Xu W. The scratch and abrasive wear behaviour of tempered martensitic construction steel and its dual phase variants. Wear 2016;358–359:80–8.

[3] Mezlini S, Ben Tkaya M, El Mansori M, Zahouani H, Kapsa Ph. Correlation between tribological parameters and wear mechanisms of homogeneous and heterogeneous material. Tribol Lett 2009;33:153–9.

[4] Cheng Q, Jiang C, Zhang J, Yang Z, Zhu Z, Jiang H. Effect of thermal aging on the scratch behavior of poly (methyl methacrylate). Tribol Int 2016;101:110–4.

[5] Zhu Z, Cheng Q, Jiang C, Zhang J, Jiang H. Scratch behavior of the aged hydrogenated nitrile butadiene rubber. Wear 2016;352–353:155–9.

[6] Gyawali G, Joshi B, Tripathi K, Lee SW. Preparation of Ni–W–Si₃N₄ composite coating sand evaluation of their scratch resistance properties. Ceram Int 2016;2:3497–503.

[7] Carrión-Vilches FJ, González-Vivas A, Martínez-Mateo IJ, Bermúdez MD. Study of the abrasion resistance under scratching of polybutylenetereftalate-glass fiber composites. Tribol Int 2015;92:365–78.

[8] Kim Sung Soo, Shin Min Wook, Jang Ho. Tribological properties of short glass fiber reinforced polyamide 12 sliding on medium carbon steel. Wear 2012;274–275:34–42.

[9] Quintelier J, De Baets P, Samyn P, Van Hemelrijck D. On the SEM features of glass–polyester composite system subjected to dry sliding wear. Wear 2006;261:703–14.

[10] Shibata Kei, Yamaguchi Takeshi, Tatsuhiro Urabe, Hokkirigawa Kazuo. Experimental study on microscopic wear mechanism of copper/carbon/rice bran ceramics composites. Wear 2012;294–295:270–6.

[11] Iqbal T, Briscoe BJ, Luckham PF. Scratch deformations of poly (etheretherketone). Wear 2011;271:1181–93.

[12] Kato Koji. Micro-mechanisms of wear–wear modes. Wear 1992;153:277–95.

[13] Briscoe BJ, Evans ED. Scratch hardness as an evaluation of cure temperature for glass fibre reinforced polyester. Compos Sci Technol 1989;34:73–90.

[14] Ben Tkaya M, Zidi M, Mezlini S, Zahouani H, Kapsa Ph. Influence of the attack angle on the scratch testing of an aluminium alloy by cones: experimental and numerical studies. Mater Des 2008;29:98–104.

[15] Meneses-Amador A, Jiménez-Tinoco LF, Reséndiz-Calderon CD, Mouftiez A, Rodríguez-Castro GA, Campos-Silva I. Numerical evaluation of scratch tests on boride layers. Surf Coat Technol 2015;284:182–91.

[16] Wredenberg F, Larsson PL. Scratch testing of metals and polymers: experiments and numeric. Wear 2009;266:76–83.

[17] Bucaille JL, Felder E, Hochstetter G. Mechanical analysis of the scratch test on elastic and perfectly plastic materials with the three-dimensional finite element modeling. Wear 2001;249:422–32.

[18] Goda T, Varadi K, Friederich K, Giertzsch H. Finite element analysis of a polymer composite subjected to a sliding steel asperity: Part I. Normal fibre orientation. J Mater Sci 2002;37:1575–83.

[19] Batra RC, Gopinath G, Zheng JQ. Damage and failure in low energy impact of fiber-reinforced polymeric composite laminates. Compos Struct 2012;94:540–7.

[20] Perillo G, Grytten F, Sørbø S, Delhaye V. Numerical/experimental impact events on filament wound composite pressure vessel. Compos B 2015;69:406–17.

[21] Friedrich K, Varadi K, Goda T, Giertzsch H. Finite element analysis of a polymer composite subjected to a sliding steel asperity: Part II. Parallel and anti-parallel fibre orientations. J Mater Sci 2002;37:3497–507.

[22] Mzali S, Mezlini S, Zidi M. Effect of tribological parameters on scratch behavior of a unidirectional E-glass fiber reinforced polyester composite. Tribol Mater Surf Interfaces 2013;4:175–82.

[23] Elwasli F, Zemzemi F, Mkaddem A, Mzali S, Mezlini S. A 3D multi-scratch test model for characterizing material removal regimes in 5083-Al alloy. Mater Des 2015;87:352–62.

[24] Wang J, Liu YB, An J, Wang LM. Wear mechanism map of uncoated HSS tools during drilling die-cast magnesium alloy. Wear 2008;265:685–91.

[25] Hodzic A, Kim JK, Stachurski ZH. Nano-indentation and nano-scratch of polymer/glass interfaces. II: Model of interphases in water aged composite materials. Polymer 2001;42:5701–10.

[26] Han G, Guan Z, Li X, Zhang W, Du S. Microscopic progressive damage simulation of unidirectional composite based on the elastic–plastic theory. J Reinf Plast Compos 2015;34:232–47.

[27] Ashouri Vajari D, González C, Llorca J, Nyvang Legarth B. A numerical study of the influence of microvoids in the transverse mechanical response of unidirectional composites. Compos Sci Technol 2014;97:46–54.

[28] Ashouri Vajari D, Nyvang Legarth B, Niordson CF. Micromechanical modeling of unidirectional composites with uneven interfacial strengths. Eur J Mech A/ Solids 2013;42:241–50.

[29] Zemzemi F. Caractérisation de modèles de frottement aux interfaces pièce-outil-copeau en usinage: application au cas de l'usinage des aciers et de l'inconel 718 [PhD thesis (French version)]. Lyon – France: École Centrale de Lyon; 2007.

[30] Kim T, Oshima K, Kawada H. Impact tensile properties and strength development mechanism of glass for reinforcement fiber. J Phys Conf Ser 2013;451:012006.

[31] Johnson GR, Cook WH. A constitutive model and data for metals subjected to large strains, high strain rate and high temperature. In: American Defense Preparedness Association, Koninklijk Instituut van Ingenieurs (Netherlands), Editors. Proceedings of the 7th international symposium on Ballistics, The Hague - Netherlands. p. 541–7.

[32] Tenorio M, Pelegri AA. Interfacial debonding of glass single fiber composites using the Johnson-Cook failure model. In: ASME, Editors. Proceedings of the ASME 2013 international mechanical engineering congress and exposition, San Diego – USA. p. 7–8.

[33] Chabert E, Ershad Langroudi A, Gauthier C, Perez J. Mechanical response of amorphous and semicrystalline oly(ethylene terephthalate) and modelling in frame of quasi point defect theory. Plast Rubber Compos Process Appl 2001;30:56–67.

[34] Ashouri Vajari D. A micromechanical study of porous composites under longitudinal shear and transverse normal loading. Compos Struct 2015;125:266–76.

[35] Chamis CC. Mechanics of composite materials: past, present, and future. J Compos Technol Res ASTM 1989;1:3–14.

[36] Benzeggagh ML, Kenane M. Measurement of mixed-mode delamination fracture toughness of unidirectional glass/epoxy composites with mixed-mode bending apparatus. Compos Sci Technol 1996;56:439–49.

[37] Li J, Sen JK. Analysis of frame-to-skin joint pull-off tests and prediction of the delamination failure. In: American Institute of Aeronautics and Astronotics, Editors. Proceedings of 42nd AIAA/ASME/ASCE/AHS/ASC/structures, structural dynamics, and materials conference. Seattle – USA: IAE Inc.; 2001. p. 1–7.

[38] Li J. Three-dimensional effects in the prediction of flange delamination in composite skin-stringer pull-off specimens. J Compos Tech Res 2002;24:180–7.

[39] Turon A, Camanho PP, Costa J, Davila CG. An interface damage model for the simulation of delamination under variable-mode ratio in composite materials. Nasa Center for AeroSpace Information NASA/TM-2004-213277; 2004. p. 1–32.

[40] Dassault Systèmes SIMULIA Corp. Abaqus analysis User's Manual. Providence, RI, USA: Dassault Systèmes SIMULIA Corp.; 2012.